

Compressed Nanolamella-Stacked $\text{Ni(OH)}_2/\text{NiCo}_2\text{O}_4$ Composite as Electrode for Battery-Type Supercapacitor

Chunli Guo,^{*[a]} Huaiyan Wang,^[a] Xiaochuan Ren,^[b] Weike Zhang,^[c] Lifeng Hou,^[a] Yinghui Wei,^[a, d] and Zhongchao Bai^{*[a]}

Transition metal oxides/hydroxides as electrode materials for supercapacitors have drawn great attention in the past decades. However, the large volume expansion during the cycling always leads to capacity decrease and short cycle life. In this paper, a compressed $\text{Ni(OH)}_2/\text{NiCo}_2\text{O}_4$ nanolamellas composite grown on nickel foam is synthesized by a one-step hydrothermal method towards the enhanced performance of supercapacitors. The resulting $\text{Ni(OH)}_2/\text{NiCo}_2\text{O}_4$ composite displays unexpectedly

excellent cycle stability both in single-electrode cycling (112% after 90,000 cycles at 5 mA cm^{-2}) and hybrid supercapacitor cycling (124% after 80,000 cycles at 1 Ag^{-1}). The excellent electrochemical performances are attributed to the unique compressed nanolamella-stacked architecture, which can not only accommodate the volume expansion, but also increase the contact area between the electrode and electrolyte.

1. Introduction

Owing to the deteriorating environmental pollution and severe energy crisis, researchers and scientists have been made great efforts to exploit renewable and sustainable energy.^[1,2] However, those energy sources are generally needed energy storage devices to conquer the time and space restriction.^[3,4] Among all kinds of energy storage systems, supercapacitors have attracted particular attention owing to the high-power density, long cycling lifespan and rapid charge/discharge features.^[5,6] Unfortunately, their low energy density limits the large-scale commercial applications.^[7,8] Battery-type supercapacitor can solve this problem, by integrating the benefits of battery electrode and capacitor, which will deliver high energy densities like batteries and high power densities like capacitors.^[1,9]

Transition metal oxides/hydroxides stands out from all the candidates of electrodes owing to the high specific capacitance and relative low price. But these electrodes always show poor

cycle stability and unsatisfactory rate capability due to the large volume variation and low conductivity.^[10–12] As previous reported, a robust structural stability for these electrode materials would play critical roles in the cycling tests, especially, those electrode materials directly grown on current collector.^[13,14] For example, Qin et al. designed and fabricated $\text{Ni(OH)}_2/\text{CNTs}$ hierarchical spheres with high specific capacity (854 C g^{-1} at 2 A g^{-1} , 16% decay after 5,000 cycles at 5 A g^{-1}).^[15] Luo et al. synthesized hierarchical $\alpha\text{-Ni(OH)}_2$ grown on CNTs as a promising supercapacitor electrode could reach $2,325 \text{ F g}^{-1}$ at a sweep rate of 1 mV s^{-1} (83.6% of the capacity retention after 10,000 cycles).^[16] Zeng et al. used a soft-templating method to hydrothermally synthesize NiCo_2O_4 nanomaterials on Ni foam (92% of the capacity retention after 5,000 cycles).^[3]

Recent studies have demonstrated that two or more component active materials could display more excellent performance of supercapacitors than single material due to their synergistic effect.^[17–19] For example, Lin et al. synthesized serpent-cactus-like Co-doped $\text{Ni(OH)}_2/\text{Ni}_3\text{S}_2$ hierarchical structure composed of ultrathin nanosheets with an ultrahigh specific capacitance of 3023.4 F g^{-1} at 1 A g^{-1} .^[20] Vijay S. Kumbhar et al. designed and fabricated $\text{ZnCo}_2\text{O}_4\text{-MnO}_2$ heterostructure, whose maximum specific capacitance was $2,057 \text{ F g}^{-1}$ at 1 A g^{-1} and capacity retention rate was 96.5% after 5,000 cycles at 15 A g^{-1} .^[21] Teng et al. fabricated a zipper-like $\text{NiCo}_2\text{O}_4/\text{Ni(OH)}_2$ structure grown on multifunctional nickel foam via a one-pot hydrothermal method, which could exhibit a high specific capacity of $2,721 \text{ mF cm}^{-2}$ at 1 mA cm^{-2} and retain 86% capacity at 1 mA cm^{-2} after 10,000 cycles.^[22] Nevertheless, the supercapacitors was still leave a large improvement room including cycling stability and rate performance.^[23,24]

Herein, $\text{Ni(OH)}_2/\text{NiCo}_2\text{O}_4$ composite directly grown on Ni foam was fabricated via a one-step hydrothermal method to improve the performance of battery-type supercapacitors. $\text{Ni(OH)}_2/\text{NiCo}_2\text{O}_4$ composite electrode owned a stable three-dimensional structure, where the triangle-frustums assembled

[a] Prof. C. Guo, H. Wang, Prof. L. Hou, Prof. Y. Wei, Dr. Z. Bai
College of Materials Science and Engineering,
Taiyuan University of Technology,
Taiyuan, Shanxi, 030024, P.R. China
E-mail: Guochunli@tyut.edu.cn
baizhongchao@tyut.edu.cn

[b] Dr. X. Ren
Department of Chemical Engineering,
Tsinghua University,
Beijing 100084, P.R. China

[c] Prof. W. Zhang
College of Environment Science and Engineering,
Taiyuan University of Technology,
Jinzhong, Shanxi 030600, P.R. China

[d] Prof. Y. Wei
College of Materials Science and Engineering,
Taiyuan University of Science and Technology,
Taiyuan, Shanxi 030024, P.R. China

 Supporting information for this article is available on the WWW under
<https://doi.org/10.1002/batt.201900190>

from the compressed nanolamellas and tightly fixed onto three-dimensional compressed nanosheets. The compressed structures could expand as the electrolyte ions came in and out, providing more active sites of the electrode and thus lead to the capacity retention rate was over 100% after 90,000 cycles in the single electrode cycle test and 124% after 80,000 cycles in hybrid supercapacitor cycle test. The excellent electrochemical performance is attributed to the unique structure design, compressed nanolamella-stacked $\text{Ni(OH)}_2/\text{NiCo}_2\text{O}_4$ composite.

2. Results and Discussion

2.1. Structural and Morphological Characterizations

Figure 1 presented the schematic diagram of the $\text{Ni(OH)}_2/\text{NiCo}_2\text{O}_4$ composite growth process. First, Ni(OH)_2 particles grew on the nickel foam because of the higher concentration of Ni^{2+} (four times more than Co^{2+} concentration) although the k_{sp} of Co(OH)_2 ($k_{sp}=1.6\times10^{-15}$) and Ni(OH)_2 ($k_{sp}=2.0\times10^{-15}$) are very close. As the reaction time prolonged, Ni(OH)_2 particles continued to grow into the network-like nanosheet structure and reacted with the cobalt ions in the solution to form NiCo_2O_4 nanorods. Finally, some new Ni(OH)_2 triangle-frustums nucleated and grew onto the former generated nanosheet surface. These results are strongly supported by the FESEM images (Figure S1) of the composites synthesized at the differ-

ent reaction times of 1 h (Figure S1a), 3 h (Figure S1b) and 5 h (Figure S1c). There were only nanosheets and nanorods in Figure S1a, while in Figure S1b, some nanobulks can be observed on the side of nanosheets. In Figure S1c, the triangle-frustums structure could be clearly detected on the side of the nanosheets.

The morphologies of the synthesized $\text{Ni(OH)}_2/\text{NiCo}_2\text{O}_4$ composite were examined by FESEM. As shown in Figure 2a to 2d, one can see that the $\text{Ni(OH)}_2/\text{NiCo}_2\text{O}_4$ composite uniformly covered on NF. The high-resolution SEM images (Figure 2c and 2d) revealed that there were three kinds structures including nanorods, nanosheets and triangle-frustums grown on NF. The triangle frustums tightly grew on the nanosheet sides and the nanosheets with some nanorods tangled up with each other grew vertically on NF to form a firm network structure (Figure 2d). In addition, the average thickness of nanosheets was about 40–70 nm and the size of the triangle frustums was about 140–220 nm.

The phase of the as-prepared sample was analyzed by XRD measurement. The diffraction peaks at $2\theta=19.3^\circ, 33.3^\circ, 38.8^\circ, 52.3^\circ, 59.5^\circ, 63.1^\circ, 70.5^\circ$ and 73.2° in Figure 3a were readily indexed to the (001), (100), (011), (012), (110), (111), (003) and (201) planes of hexagonal Ni(OH)_2 (JCPDS-73-1520).^[25–27] No diffraction peaks of NiCo_2O_4 were found in Figure 3a, possibly due to their low content. So we also used the XRD to index the powder collected from the autoclave, Figure S2 was the XRD patterns of the powder collected from the autoclave, the powder contained Ni(OH)_2 and NiCo_2O_4 . The element valence

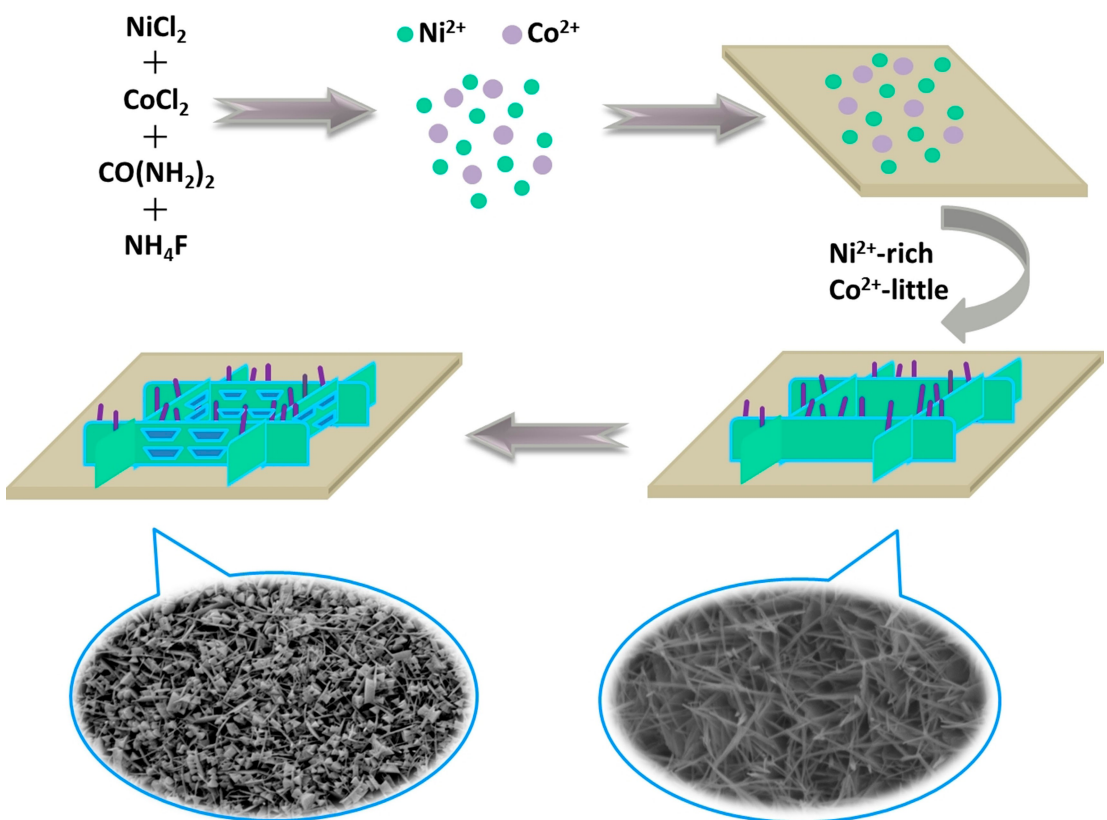


Figure 1. Schematic describing the grow process of $\text{Ni(OH)}_2/\text{NiCo}_2\text{O}_4$ composite grown on NF.

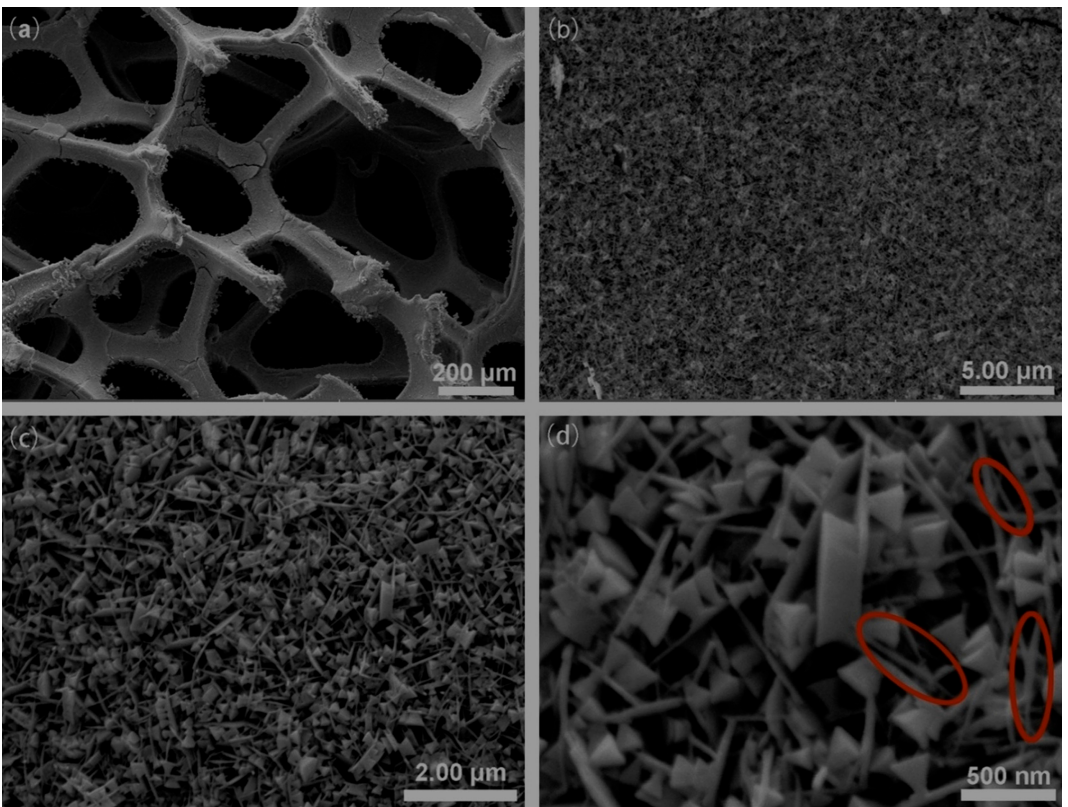


Figure 2. (a-d) FESEM images of $\text{Ni}(\text{OH})_2/\text{NiCo}_2\text{O}_4$ composite grown on NF under different resolution.

state and the chemical composition of the $\text{Ni}(\text{OH})_2/\text{NiCo}_2\text{O}_4$ composite were further characterised by XPS spectrum. Figure 3b was the full-survey-scan XPS spectra of the sample, demonstrating the presence of Ni, Co, O and C elements in the samples. The peaks at 856.4 and 875.4 eV in Figure 3c were assigned to Ni^{3+} , and those of 851.7 and 873.4 eV were assigned to Ni^{2+} , whose satellite peaks appeared at 862.1 and 880.2 eV. The fitting peaks of 787 and 803.2 eV accompanied by two satellite peaks at 782.9 and 798.7 eV corresponded to Co^{2+} and those of 781.1 and 796.8 eV indexed to Co^{3+} (Figure 3d).^[28–30]

HRTEM (Figure 4a–4c) was used to further elucidate the detailed phase structure of the composite. The visible lattice fringes of the (100) ($d=0.268 \text{ nm}$) and (003) ($d=0.154 \text{ nm}$) planes of the $\text{Ni}(\text{OH})_2$ nanosheet, the (311) ($d=0.25 \text{ nm}$) plane of the NiCo_2O_4 nanorod (JCPDS-02-1074) and the (012) ($d=0.18 \text{ nm}$) and (011) ($d=0.233 \text{ nm}$) planes of the $\text{Ni}(\text{OH})_2$ triangle-frustum were indicated in Figure 4a, Fig 4b and Figure 4c, respectively. This analysis data suggested that the nanosheets and the triangle-frustums were made of $\text{Ni}(\text{OH})_2$ and the nanorods were composed of NiCo_2O_4 . Figure 4d displayed the EELS patterns of the composite, it also further confirmed that the chemical compositions of the nanosheets and triangle-frustums were $\text{Ni}(\text{OH})_2$ and the nanorods were belonged to NiCo_2O_4 . Figure 4a₁ depicted the HAADF-STEM image of the nanosheet, which EDX element map showed the spatial distributions of the atomic contents and confirmed the presence of only Ni and O atoms in the nanosheet (a₂ and a₃).

Figure 4b₁ represented the HAADF-STEM image of the nanorod, which EDX element map proved the presence of Co, Ni and O atoms in the nanorod (b₂ and b₄). The analysis results of the triangle frustums were similar to the nanosheets (c₁–c₃). The results agreed with EELS. Therefore, the product was composed of the $\text{Ni}(\text{OH})_2$ nanosheets/ triangle-frustums and NiCo_2O_4 nanorods.

2.2. Electrochemical Performance of Single Electrode

The electrochemical performances of $\text{Ni}(\text{OH})_2/\text{NiCo}_2\text{O}_4$ composite were evaluated by CV and GCD in 6 M KOH. Figure 5a was displayed the CV curves of $\text{Ni}(\text{OH})_2/\text{NiCo}_2\text{O}_4$ electrode at different scan rates, which all shared a similar shape with a pair of the obvious redox peaks, indicating a good rate capability of the composite.^[31] It is noteworthy that the variations in redox peak position between low and high scan rate was only 0.023–0.027 V, which is much less than those of other similar materials (0.05–0.1 V or more),^[9,32,33] demonstrating the faster electrochemical behavior of this electrode.^[34] Figure 5b showed the GCD curves at various current densities from 2 to 10 mA cm^{-2} . All curves exhibited nearly symmetric appearance, implying a high coulombic efficiency, and which is the typical charge-discharge plateaus of the battery-type electrode.^[35] Additionally, the electrode displayed an areal specific capacity of 140 mC cm^{-2} at 2 mA cm^{-2} and 104 mC cm^{-2} even at high current of 10 mA cm^{-2} , showing a good rate capability.

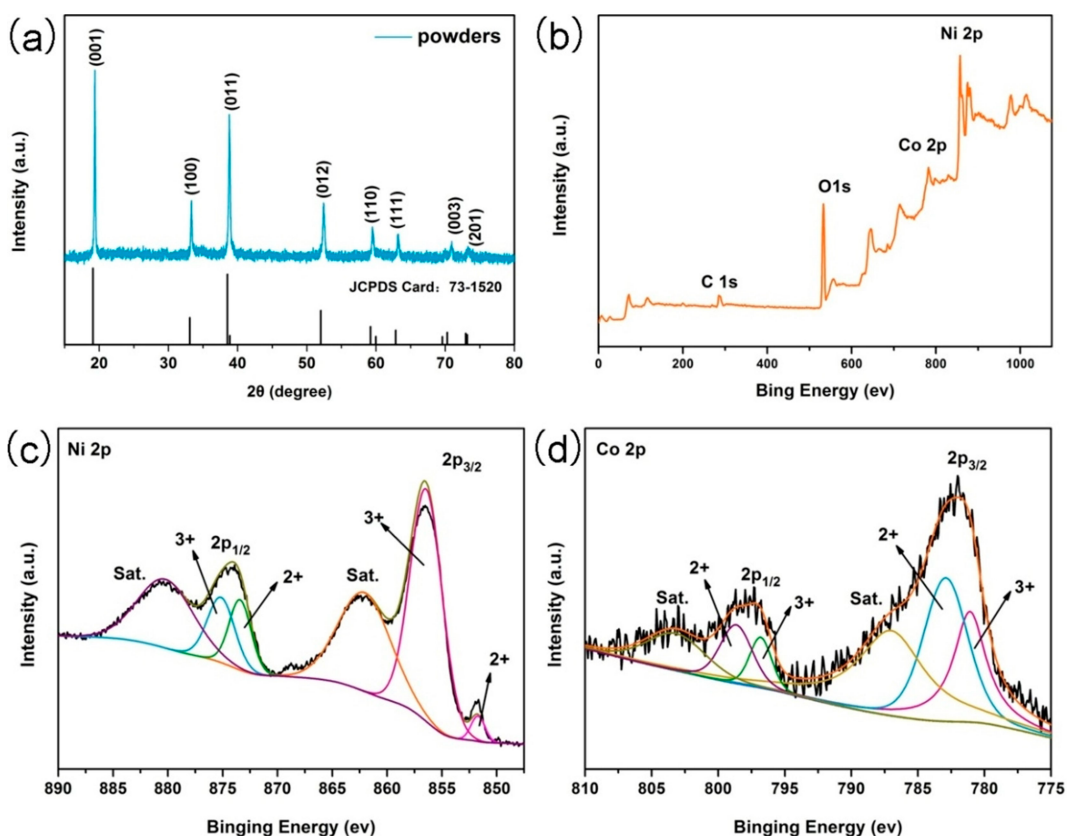


Figure 3. (a) XRD patterns of the powder on NF; (b) the full-survey-scan XPS spectra of the composite; (c) high-resolution XPS spectra of Ni 2p; (d) high-resolution XPS spectra of Co 2p.

Long cycling lifespan was one of the most important factors for supercapacitors to realize their commercialization. Therefore, the continuous charge/discharge test (Figure 5c) was carried out for the $\text{Ni(OH)}_2/\text{NiCo}_2\text{O}_4$ electrode at 5 mA cm^{-2} for 90,000 cycles. The capacity retention rate showed a slightly upward trend up to 130% during the first 20,000 cycles owing to the electrode material activation and an increase of activation sites, and then stabilized at about 110% after 65,000 cycles.^[36,37] Even after 90,000 cycles, the capacity retention rate was still 112%. An Nyquist plot of the $\text{Ni(OH)}_2/\text{NiCo}_2\text{O}_4$ electrode was used to compare the resistance difference before and after 90,000 cycles, and shown in Figure 5d. The intrinsic resistance (R_s) of the electrode decreased from 0.84 to 0.06 Ω after 90,000 cycles, implying the reduce resistance for the whole electrode. The semi-cycle diameter in the high frequency region after the long-term cycle was far less than that of before cycle, showing the smaller charge-transfer resistance. The curve slope in the low frequency region after the long-term cycle was increased, indicating the lower resistance for ion/proton diffusion. In conclusion, the resistances including the electrode resistance, the charge-transfer resistance and the ion/proton diffusion resistance were all reduced as the cycling proceeding, and thus resulting in the outstanding cycling stability of the $\text{Ni(OH)}_2/\text{NiCo}_2\text{O}_4$ electrode.^[35]

Generally, the morphology of the electrode material made a big difference on the electrode behavior.^[38,39] Therefore, the

correlation between the cycling stability and the morphology of the composite electrode were detected by FESEM after 10,000 cycles. The integral morphology of the electrode material did not change significantly during cycling (Figure S4a). However, the high-resolution SEM image (Figure S4b) displayed that the nanosheets and the triangle-frustums of the electrode material were expanded into multilayer structures with thinner nanolamellas after 10,000 cycles. It was the unceasing insertion/intercalation of OH^- between the layered Ni(OH)_2 material during the cycling process that led to the multilayer structure formation and the exposure of more active sites to participate in electrochemical reactions, which ultimately brought about the capacity increases. Furthermore, the multilayer structures in 3D network architecture were firm enough so that they could reduce the stress generated by the ion insertion/intercalation because of the expanded triangle-frustum structure support, which gave rise to an excellent structural stability and an ultra-long cycle life. The lower resistance after 90,000 cycling was to a large extent related to the special ultra-thin lamellar structure morphology of the electrode material which shortened the distance of charge/ion/proton transport.^[40–42]

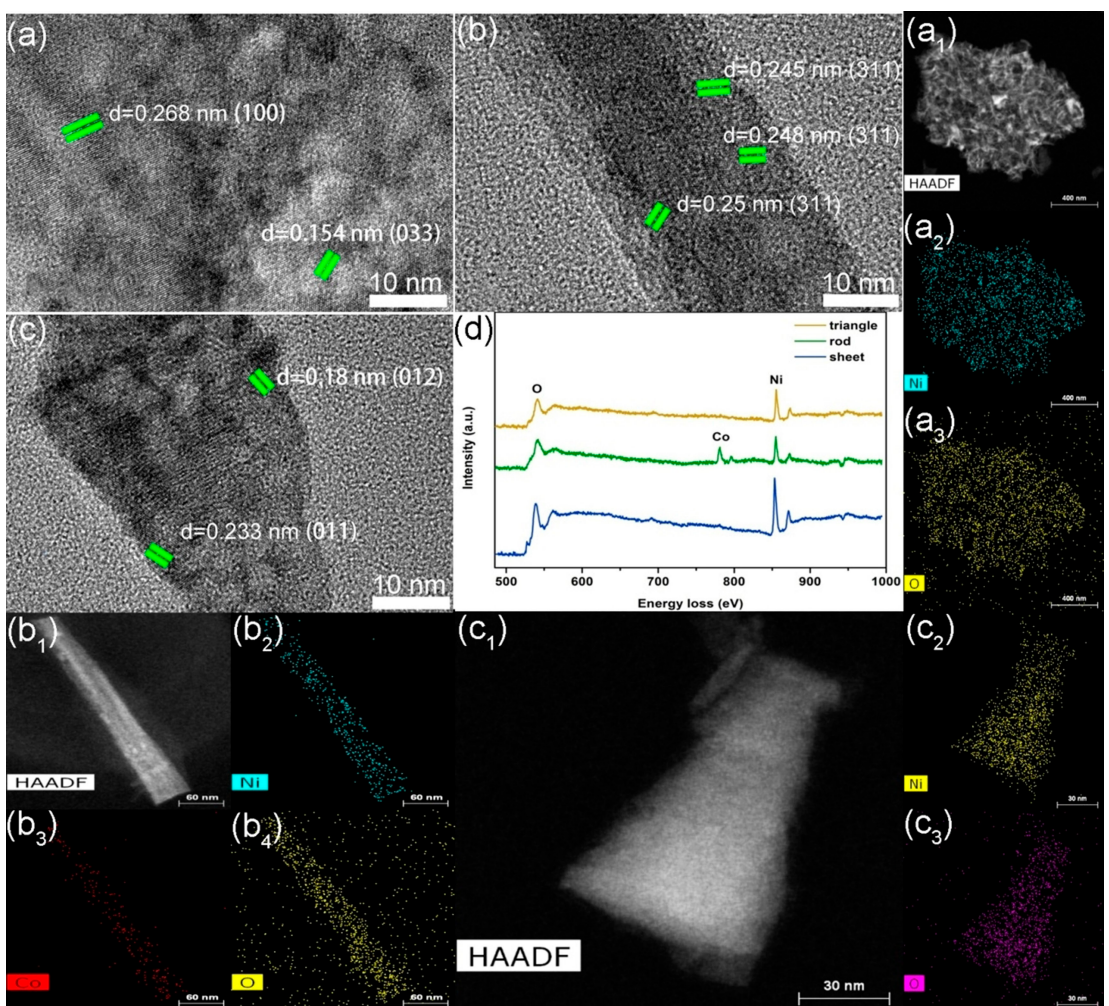


Figure 4. (a–c) HRTEM images of the composite: (a) nanosheet, (b) nanorod, (c) nanotriangle; (d) EELS patterns of the composite, HAADF-STEM and the corresponding EDX mappings images of the nanosheet (a₁–a₃), nanorod (b₁–b₄), triangle frustums (c₁–c₃).

2.3. Electrochemical Performance of Aqueous Hybrid Supercapacitor

In order to evaluate the practical application of the composite, we assembled an aqueous hybrid supercapacitor by using $\text{Ni(OH)}_2/\text{NiCo}_2\text{O}_4$ composite as the positive electrode and AC as the negative electrode. When the voltage window was set as 0–1.6 V, a significant polarization phenomenon occurred. Therefore, the test voltage window for the hybrid capacitor was chosen in the range of 0–1.5 V (Figure S3).^[43,44] Figure 6a was the CV curves measured at the scan rate ranging from 10 to 50 mVs⁻¹. The similar CV curves collected at different scan rates, demonstrating the excellent rate performance of the hybrid supercapacitor. The GCD curve about the potential versus time profiles at different current densities was shown in Figure 6b, where the symmetric curve is agreement with the CV test. The specific capacity calculated based on GCD was 36.3 Cg⁻¹ at 0.05 Ag⁻¹. As shown in Figure 6c, the capacity retention rate of HSC increased to 160% at 1 Ag⁻¹ after 40,000 cycles and then decreased to 124% after 80,000 cycles, exhibiting good cycle stability. From Figure 6d, one could see

that the intrinsic resistance of the cell decreased after cycle process, which is in consistent with that in the single electrode system.

Also, the FESEM images of the samples after 80,000 cycles were displayed in Figure S5. Interestingly, the overall morphology of the composite didn't change, and the original structures were also transformed into multilayer-type. Compared with Figure S4a and Figure S5c, we found that the space among the nanolamellas of nanosheet became larger after 80,000 cycles, close to that of the triangle-frustum nanolamellas. Hence the triangle frustums were firmly fixed on the side of Ni(OH)_2 nanosheets could only expand into multilayer-type structure in a limited space of the network-like nanosheets. Moreover, the network-like nanosheet expansion into the multilayer structure was also limited into the remaining space of the triangle frustums. Therefore, the nanolamellas network structure between the Ni(OH)_2 nanosheets and the Ni(OH)_2 triangle frustums supported by each other formed after the long-term cycle, resulting in the stable structure formation. Figure S5d was the high-resolution SEM image, which showed many holes of similar size covered on NF after 80,000 cycles. In the process

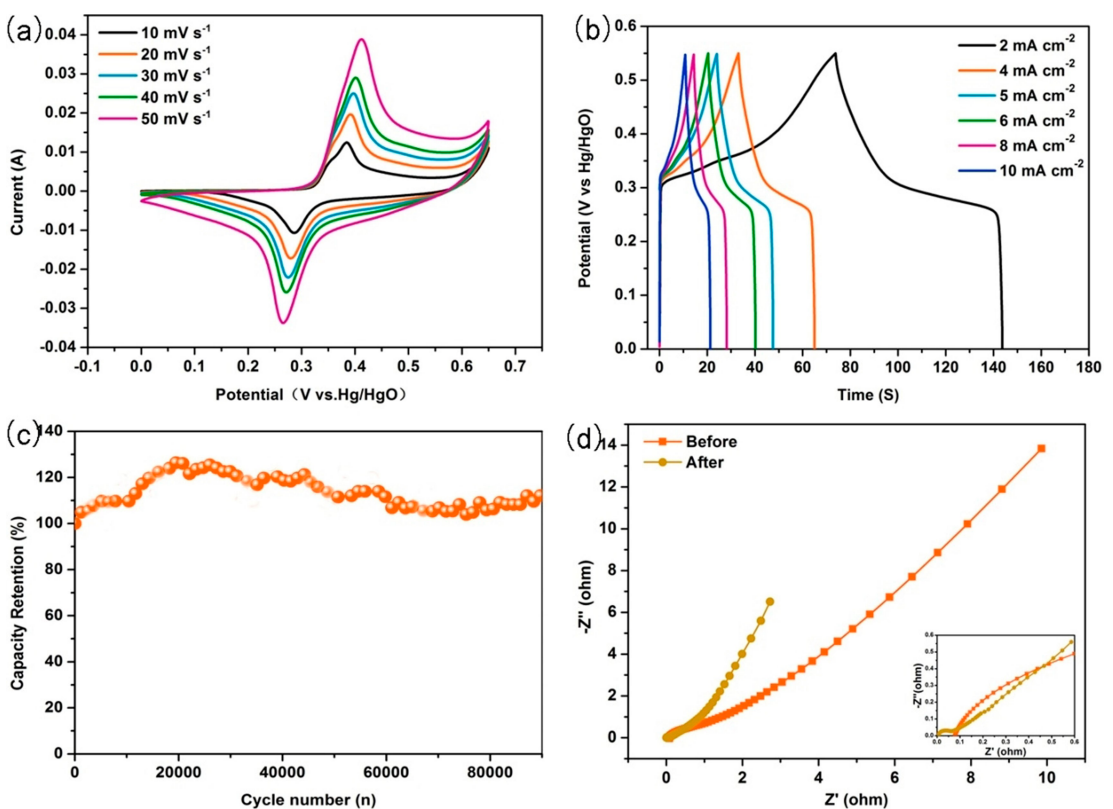


Figure 5. (a) CV cycles of the $\text{Ni}(\text{OH})_2/\text{NiCo}_2\text{O}_4$ composite electrode at various scan rates in 6 M KOH; (b) GCD curves of the electrode at various current densities; (c) Cycling performance of the electrode for 90,000 cycles; (d) EIS of the electrode after 1 and 90,000 cycles tests.

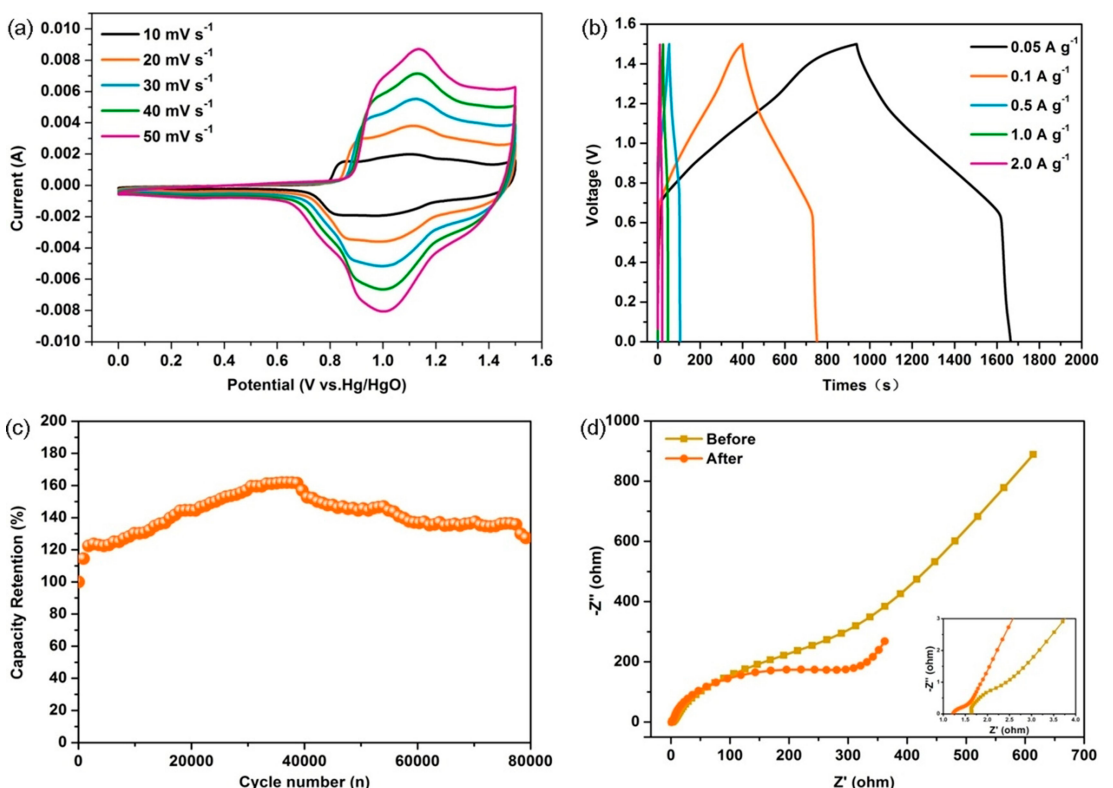


Figure 6. (a) CV cycles of HSC at various scan rates; (b) GCD curves of HSC at various current densities; (c) Cycling performance of HSC for 80,000 cycles; (d) EIS of HSC after 1 and 80,000 cycles tests.

of ion insertion/intercalation, the Ni(OH)_2 nanosheets/triangle-frustums expanded into a 3D porous material, similar to the KOH activation of carbon-based materials.^[45–47] The expandable 3D materials not only provided abundant adsorption sites to improve the utilization of active material but also the ultra-thin nanolamellas further shortened the distances of ion diffusion and enhanced electron conduction to improve the kinetics of the reaction of the electrode materials. Importantly, the structure flexibility could tolerate the structure distortion stress.^[48,49]

The structural changes after long-term cycles were examined by STEM and shown in Figure 7a and 7b, where clearly demonstrated that the ultrathin nanosheets still kept their original shape. The interplanar distance of 0.203 and 0.144 nm in Figure 7c corresponded to the (400) and (440) planes of the NiCo_2O_4 and the interplanar distance of 0.23 nm in Figure 7d belonged to the Ni(OH)_2 . Figure 7e was the elemental mapping analyses performed by HAADF-STEM-EDX. We could see that the Ni, Co, O and K elements were distributed homogeneously in entire region. Of which, the existence of K had two possibilities: one was the residual K^+ on the electrode upper surface after cycling and the other was the K^+ going into the layered structure during cycle process which was difficult to be washed out. Hence we soaked the cycled electrode materials in deionized water and ethanol for a long time to remove the K^+ , then characterized by XPS (Figure S6). There was no the existence of K^+ after soaking, showing K^+ entering the lamellar nanosheets (Fig S6b). The adsorption of K^+ among the nanolamellas was beneficial to attract OH^- and improved the electrochemical performances.

In short, this composite electrode would be activated during the cycling process and its structure changed from the compressed nanolamellas to the expanded multilayers. There was an obvious volume expansion in the cyclic process, but it did not destroy the whole structure of the electrode and promoted the stress release of the electrode morphology changes. Furthermore, the multilayer-type nanolamella struc-

ture with the coexistence of holes and lamellar sheets could expose more active sites and prompt fast charge/ion/proton transport, resulting in the increase of the capacity and the enhance of cycle stability (Figure 8).

3. Conclusions

In summary, the compressed nanolamella-stacked $\text{Ni(OH)}_2/\text{NiCo}_2\text{O}_4$ composite on NF fabricated by one-step hydrothermal method, which will be expanded through KOH-activating after long-term cycling because of ions in/out. Interestingly, this expansion did not destroy the electrode structure but enhanced its cycle stability. Consequently, the sample delivered an extremely long lifespan with high capacity retention rate of 112% after 90,000 cycles at 5 mA cm^{-2} . When it was used the positive electrode for hybrid supercapacitor, the retention rate of capacity was 124% at 1 A g^{-1} after 80,000 cycles, and the energy density was 7.56 Wh kg^{-1} at a power density 37.5 W kg^{-1} . This electrode material with ultra-long cycle lifetime could stand as candidate for the commercial application of hybrid supercapacitors.

Experimental Section

Synthesis of $\text{Ni(OH)}_2/\text{NiCo}_2\text{O}_4$ composite on Ni foam

In a typical experimental procedure, nickel foam (NF, 1 × 5 cm^{-2}) was sonicated in 2 M HCl for 15 minutes to remove the oxides on the surface, and subsequently washed by ethanol and deionised water several times. Then, the treated nickel foam was placed in a Teflon autoclave of 60 mL capacity. Afterwards, a 40 mL solution with $\text{CoCl}_2 \cdot 6\text{H}_2\text{O}$ (0.25 mmol), $\text{NiCl}_2 \cdot 6\text{H}_2\text{O}$ (1 mmol), $\text{CO}(\text{NH}_2)_2$ (6.25 mmol) and NH_4F (1.25 mmol) was transferred into the above autoclave, and sealed, and heated at 180 °C for 6 h. After the autoclave cooled to room temperature, the nickel foam with active substance was washed with deionised water and ethanol several times and dried at 60 °C for 12 h. To study the growth process,

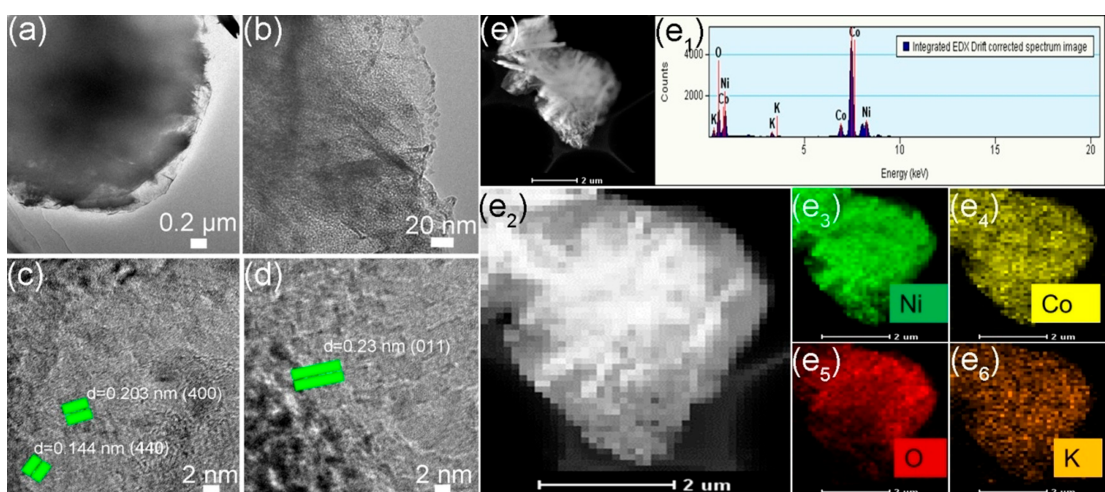


Figure 7. $\text{Ni(OH)}_2/\text{NiCo}_2\text{O}_4$ composite electrode after 80,000 cycles in two-electrode cycling of (a–b) TEM images; (c–d) HRTEM images; (e) HAADF-STEM images; (e₁) EDX patterns and (e₂–e₆) STEM-EDS images.

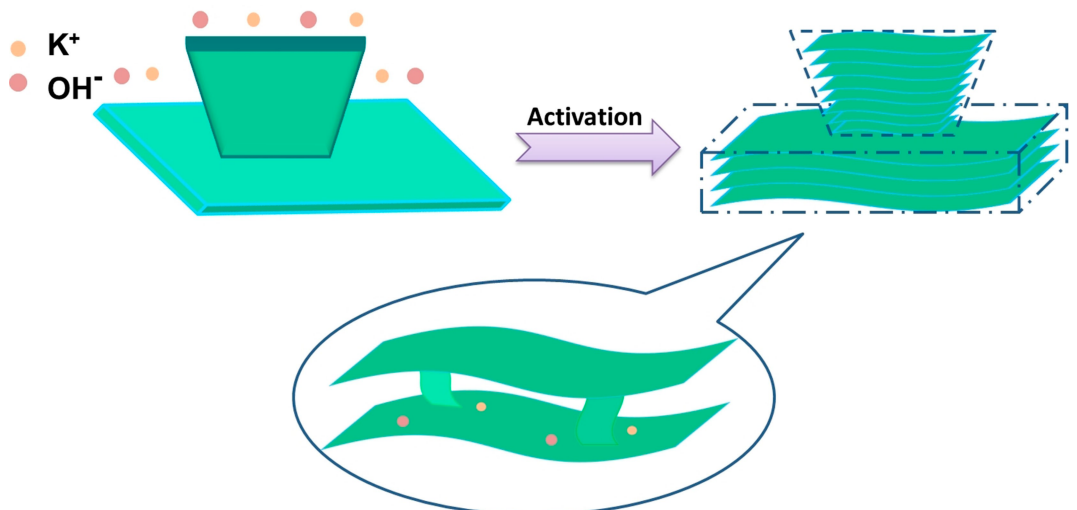


Figure 8. Schematic describing the $\text{Ni}(\text{OH})_2/\text{NiCo}_2\text{O}_4$ composite after KOH activation.

other $\text{Ni}(\text{OH})_2/\text{NiCo}_2\text{O}_4$ composite materials were also synthesized under the same reaction condition except the reaction time.

Preparation of aqueous hybrid supercapacitor

The aqueous hybrid supercapacitor was assembled using $\text{Ni}(\text{OH})_2/\text{NiCo}_2\text{O}_4$ composite as the positive electrode, active carbon (AC) as the negative electrode and polypropylene as the separator in 6 M KOH electrolyte. The optimal mass ratio of positive/negative electrodes was calculated using Equation (1):

$$\frac{m_+}{m_-} = \frac{C_- \Delta V_-}{C_+ \Delta V_+} \quad (1)$$

where C_+ , C_- , m_+ , m_- , ΔV_+ and ΔV_- are the specific capacity (Cg^{-1}), mass (g) and working voltage window (V) of positive and negative electrodes respectively. To prepare negative electrodes, a mixture (8:1:1) of activated carbon, acetylene black and poly tetra fluoroethylene (PTFE) was well mixed and formed a homogeneous slurry, and then coated on the nickel foam with a size of $1 \times 1 \text{ cm}^2$ and dried in a vacuum oven at 60°C for 12 h.

Material characterisation

The phase characteristics of the as-prepared samples were identified by X-ray diffraction (XRD, Bruker D8, Cu $\text{K}\alpha$ radiation, $\lambda = 0.15418 \text{ nm}$). The elemental chemical state of the products was examined by X-ray photoelectron spectroscopy which recorded on an Axis Ultra (Kratos, UK) spectrometer, using a standard Al $\text{K}\alpha$ X-ray source (150 W) and an analyzer pass energy of 30 eV. The morphologies and the elemental mappings of the products were observed by a field-emission scanning electron microscope (FESEM, SU8000, 5 KV), high resolution transmission electron microscopy (HRTEM, JEOL 2100F, 200 kV) equipped with energy dispersive X-ray spectroscopy (EDS), high angle annular dark field canning transmission electron microscopy (HAADF-STEM) and electron energy loss spectroscopy (EELS).

The electrochemical measurements were carried out using CHI 660E workstation in 6 M KOH aqueous electrolyte. In the single electrode electrochemical test, the as-prepared electrode, Hg/HgO and platinum foil ($2 \times 2 \text{ cm}^2$) was used as working electrode,

reference electrode and counter electrode, respectively. Cyclic voltammetry (CV) was tested from 0.0 to 0.65 V at different scanning rates. Galvanostatic charge-discharge (GCD) tests ran from 0.0 to 0.55 V at different current densities. Electrochemical impedance spectroscopy (EIS) was measured from 100 kHz to 0.01 Hz.

The specific capacity calculations were carried out using Equations (2)-(5):

$$C_A = \frac{I \Delta t}{S} \quad (2)$$

$$C_s = \frac{I \Delta t}{m} \quad (3)$$

$$E = \frac{C_s \Delta V}{2 \times 3.6} \quad (4)$$

$$P = \frac{E \times 3600}{\Delta t} \quad (5)$$

where C_A (Ccm^{-2}) is the areal specific capacity, C_s (Cg^{-1}) is the specific capacity, I (A) is the discharge current, S (cm^{-2}) refers to surface area of the electrode, m (g) is the mass of the electrode, Δt (s) stands for the discharge time, E (Wh kg^{-1}) is the energy density and P (Wkg^{-1}) is the power density.

Acknowledgements

The authors acknowledge the National Natural Science Foundation of Shanxi Province (201801D121280) and Key R&D Projects of Shanxi Province (Social Development Field, 201803D31049) for providing funding support to the current work.

Conflict of Interest

The authors declare no conflict of interest.

Keywords: transition metal oxides/hydroxides • Ni(OH)₂/NiCo₂O₄ composite • battery-type supercapacitor • energy storage

- [1] Y. Y. Zhu, C. H. Huang, C. Li, M. Q. Fan, K. Y. Shu, H. C. Chen, *J. Power Sources* **2019**, *412*, 559–567.
- [2] J. X. Nan, Y. Shi, Z. Q. Xiang, S. Wang, J. W. Yang, B. Zhang, *Electrochim. Acta* **2019**, *301*, 107–116.
- [3] Z. Z. Zeng, L. Z. Zhu, E. S. Han, X. C. Xiao, Y. R. Yao, L. M. Sun, *Ionics* **2019**, *25*, 2791–2803.
- [4] Y. L. Liu, C. Yan, G. G. Wang, H. Y. Zhang, L. Y. Dang, B. W. Wu, Z. Q. Lin, X. S. An, J. C. Han, *ACS Appl. Mater. Interfaces* **2019**, *11*, 9984–9993.
- [5] L. Zhang, L. Dong, M. X. Li, P. Wang, J. J. Zhang, H. B. Lu, *J. Mater. Chem. A* **2018**, *6*, 1412–1422.
- [6] M. S. Wu, J. X. Xu, *Electrochim. Acta* **2019**, *319*, 31–40.
- [7] T. Dang, L. Wang, D. H. Wei, G. Q. Zhang, Q. G. Li, X. J. Zhang, Z. Y. Cao, G. H. Zhang, H. G. Duan, *Electrochim. Acta* **2019**, *299*, 346–356.
- [8] Y. Yang, S. Li, W. Huang, H. H. Shangguan, C. Engelbrekt, S. W. Duan, L. J. Ci, P. C. Si, J. Mater. Chem. A **2019**, *7*, 14670–14680.
- [9] Q. Zong, H. Yang, Q. Q. Wang, Q. L. Zhang, Y. L. Zhu, H. Y. Wang, Q. H. Shen, *Chem. Eng. J.* **2019**, *361*, 1–11.
- [10] L. X. Zheng, L. T. Guan, J. L. Song, H. J. Zheng, *Appl. Surf. Sci.* **2019**, *480*, 727–737.
- [11] H. G. Li, A. F. Liu, H. W. Che, *Mat. Sci. Semicon. Proc.* **2019**, *91*, 115–123.
- [12] C. Yang, M. J. Shi, Y. Y. Tian, J. Yang, X. F. Song, L. P. Zhao, J. Liu, P. Zhang, L. Gao, *J. Mater. Chem. A* **2019**, *7*, 3432–3442.
- [13] T. Wang, H. C. Chen, F. Yu, X. S. Zhao, H. X. Wang, *Energy Storage Mater.* **2019**, *16*, 545–573.
- [14] I. Hussain, A. Ali, C. Lamiel, S. G. Mohamed, S. Sahoo, J. J. Shim, *Dalton Trans.* **2019**, *48*, 3853–3861.
- [15] Q. Qin, J. Liu, W. Mao, C. Xu, B. Lan, Y. Wang, Y. Zhang, J. Yan, Y. Wu, *Nanoscale* **2018**, *10*, 7377–7381.
- [16] Y. Luo, Y. G. Li, D. X. Wang, C. B. Zhai, T. Y. Yang, M. Z. Zhang, *J. Alloys Compd.* **2018**, *743*, 1–10.
- [17] X. M. Wu, M. Lian, Q. G. Wang, *Electrochim. Acta* **2019**, *295*, 655–661.
- [18] L. L. Tian, K. D. Xia, S. P. Wu, Y. H. Cai, H. D. Liu, X. L. Jing, T. Yang, D. D. Chen, X. Bai, M. Zhou, L. Li, *Electrochim. Acta* **2019**, *307*, 310–317.
- [19] J. J. Zhou, X. Han, K. Tao, Q. Li, Y. L. Li, C. Chen, L. Han, *Chem. Eng. J.* **2018**, *354*, 875–884.
- [20] L. Ye, L. J. Zhao, H. Zhang, P. Zan, S. Gen, W. H. Shi, B. Han, H. M. Sun, X. J. Yang, T. H. Xu, *J. Mater. Chem. A* **2017**, *5*, 1603–1613.
- [21] V. S. Kumbhar, D. H. Kim, *Electrochim. Acta* **2018**, *271*, 284–296.
- [22] Y. Teng, Y. Q. Huo, S. T. Li, X. M. Niu, N. Fan, Z. M. Su, *J. Alloys Compd.* **2019**, *784*, 712–719.
- [23] Y. L. Shao, M. F. El-Kady, J. Y. Sun, Y. G. Li, Q. H. Zhang, M. F. Zhu, H. Z. Wang, B. Dunn, R. B. Kaner, *Chem. Rev.* **2018**, *118*, 9233–9280.
- [24] Z. Lin, E. Goikolea, A. Balducci, K. Naoi, P. L. Taberna, M. Salanne, G. Yushin, P. Simon, *Mater. Today* **2018**, *21*, 419–436.
- [25] B. J. Rani, N. Dhivya, G. Ravi, S. S. Zance, R. Yuvakkumar, S. I. Hong, *ACS Omega* **2019**, *4*, 10302–10310.
- [26] S. Saffarzadeh, G. Nabiyouni, D. Ghanbari, *J. Mater. Sci. Mater. Electron.* **2016**, *27*, 13338–13350.
- [27] B. L. Lv, Z. Liu, R. M. Ding, D. Wu, Y. Xu, *J. Mater. Chem. A* **2013**, *1*, 5695–5699.
- [28] C. L. Guo, J. Li, Y. T. Chu, H. B. Li, H. P. Zhang, L. F. Hou, Y. H. Wei, J. Liu, S. L. Xiong, *Dalton Trans.* **2019**, *21*, 2019–2027.
- [29] S. X. Cui, T. T. Li, C. L. Guo, L. L. Wang, C. C. Zhang, Z. Y. Yan, Y. H. Wei, L. F. Hou, L. C. Xu, C. K. Jia, *J. Nanosci. Nanotechnol.* **2019**, *19*, 47–56.
- [30] W. Q. Chen, J. Wang, K. Y. Ma, M. Li, S. H. Guo, F. Liu, J. P. Cheng, *Appl. Surf. Sci.* **2018**, *451*, 280–288.
- [31] Q. S. Nian, S. Liu, J. Liu, Q. Zhang, J. Q. Shi, C. Liu, R. Wang, Z. L. Tao, J. Chen, *ACS Appl. Energy Mater.* **2019**, *2*, 4370–4378.
- [32] Q. Y. Zhou, T. W. Fan, Y. Y. Li, D. C. Chen, S. L. Liu, X. Li, *J. Power Sources* **2019**, *426*, 111–115.
- [33] P. Xia, Q. Y. Wang, Y. T. Wang, W. Quan, D. L. Jiang, M. Chen, *J. Alloys Compd.* **2019**, *771*, 784–792.
- [34] F. E. Sarac, Oztuna, U. Unal, *Solid-State Electron.* **2019**, *23*, 1409–1417.
- [35] Q. Y. Zhou, J. P. Huang, C. Y. Li, Z. W. Lv, H. L. Zhu, G. Hu, J. New, *Chem.* **2019**, *43*, 5904–5913.
- [36] Y. Zhang, L. Yu, R. D. Hu, J. L. Zhang, Y. N. Wang, R. C. Niu, X. Y. Qian, J. W. Zhu, *J. Mater. Chem. A* **2018**, *6*, 17417–17425.
- [37] Y. F. Ai, X. W. Geng, Z. Lou, Z. M. Wang, G. Z. Shen, *ACS Appl. Mater. Interfaces* **2015**, *7*, 24204–24211.
- [38] X. C. Ren, C. L. Guo, L. Q. Xu, T. T. Li, L. F. Hou, Y. H. Wei, *ACS Appl. Mater. Interfaces* **2015**, *7*, 19930–19940.
- [39] G. W. Yang, C. L. Xu, H. L. Li, C. L. Xu, *Chem. Commun. (Camb.)* **2008**, *48*, 6537–6539.
- [40] J. H. Zhong, A. L. Wang, G. R. Li, J. W. Wang, Y. N. Ou, Y. X. Tong, *J. Mater. Chem.* **2012**, *22*, 5656–5665.
- [41] Y. F. Yuan, X. H. Xia, J. B. Wu, J. L. Yang, Y. B. Chen, S. Y. Guo, *Electrochim. Acta* **2011**, *56*, 2627–2632.
- [42] X. J. Ma, L. B. Kong, W. B. Zhang, M. C. Liu, Y. C. Luo, L. Kang, *RSC Adv.* **2014**, *4*, 17884–17890.
- [43] Y. Liu, N. Q. Fu, G. G. Zhang, M. Xu, W. Lu, L. M. Zhou, H. T. Huang, *Adv. Funct. Mater.* **2017**, *27*, 1605307.
- [44] D. X. Guo, L. Zhang, X. M. Song, L. C. Tan, H. Y. Ma, J. Jiao, D. Zhu, F. B. Li, J. New, *Chem.* **2018**, *42*, 8478–8484.
- [45] S. L. Wu, G. X. Chen, N. Y. Kim, K. N. W. C. Zeng, Y. Zhao, Z. C. Tao, H. X. Ji, Z. H. Lee, Y. W. Zhu, *Small* **2016**, *12*, 2376–2384.
- [46] Y. Gao, Y. S. Zhou, M. Qian, X. N. He, J. Redepenning, P. Goodman, H. M. Li, L. Jiang, Y. F. Lu, *Carbon* **2013**, *51*, 52–58.
- [47] J. S. Zhang, J. W. Lee, *ACS Sustainable Chem. Eng.* **2014**, *2*, 735–740.
- [48] H. Chen, L. F. Hu, M. Chen, Y. Yan, L. M. Wu, *Adv. Funct. Mater.* **2014**, *24*, 934–942.
- [49] Y. M. Lv, A. F. Liu, H. W. Che, J. B. Mu, Z. C. Guo, X. L. Zhang, Y. M. Bai, Z. X. Zhang, G. S. Wang, Z. Z. Pei, *Chem. Eng. J.* **2018**, *336*, 64–73.

Manuscript received: November 22, 2019

Revised manuscript received: December 16, 2019

Accepted manuscript online: December 23, 2019

Version of record online: February 3, 2020